

See discussions, stats, and author profiles for this publication at: <https://www.researchgate.net/publication/216776270>

# Study of Redox Species and Oxygen Vacancy Defects at TiO<sub>2</sub>–Electrolyte Interfaces

ARTICLE in THE JOURNAL OF PHYSICAL CHEMISTRY C · NOVEMBER 2010

Impact Factor: 4.77 · DOI: 10.1021/jp107385e

CITATIONS

28

READS

33

6 AUTHORS, INCLUDING:



**Robson da Silva**

Federal University of Santa Catarina

9 PUBLICATIONS 98 CITATIONS

SEE PROFILE



**L. G. C. Rego**

Federal University of Santa Catarina

58 PUBLICATIONS 1,432 CITATIONS

SEE PROFILE



**Daniel Laria**

University of Buenos Aires

71 PUBLICATIONS 1,267 CITATIONS

SEE PROFILE

Study of Redox Species and Oxygen Vacancy Defects at TiO<sub>2</sub>–Electrolyte Interfaces

Robson da Silva,<sup>†</sup> Luis G. C. Rego,<sup>\*,‡</sup> José A. Freire,<sup>¶</sup> Javier Rodriguez,<sup>§</sup> Daniel Laria,<sup>§</sup> and Victor S. Batista<sup>||</sup>

Department of Chemistry, Universidade Federal de Santa Catarina, Florianópolis, SC 88040-900, Brazil,

Department of Physics, Universidade Federal de Santa Catarina, Florianópolis, SC 88040-900, Brazil,

Department of Physics, Universidade Federal do Paraná, Curitiba, PR 81531-990, Brazil, Department of

Physics, Comisión Nacional de Energía Atómica, Avenida Libertador 8250, 1429 Buenos Aires, Argentina,

and Department of Chemistry, Yale University, P.O. Box 208107, New Haven, Connecticut 06520-8107

Received: August 5, 2010; Revised Manuscript Received: September 21, 2010

The structural, energetic, and electronic properties of the TiO<sub>2</sub>–electrolyte interface in dye-sensitized solar cells is studied by molecular dynamics simulations and electronic structure calculations. The investigation enlightens the mechanisms responsible for the recombination of photoelectrons with redox species in the electrolyte (back-reaction effect), taking into account the important influence of surface defects, the underlying solvent dynamics, and the presence of pyridine additives at the interface. The free-energy barrier for the adsorption of redox species at the TiO<sub>2</sub> surface is calculated. Electronic structure calculations of the TiO<sub>2</sub>/redox/solvent system evidence the distinct recombination mechanisms for the different redox species. The study provides a deeper insight on the molecular processes taking place at the interface and should stimulate further theoretical and experimental investigations.

## 1. Introduction

Understanding semiconductor–electrolyte interfaces at the molecular level is a central problem common to a wide range of technological applications, including the development of efficient dye-sensitized solar cells (DSSCs).<sup>1–5</sup> It is well-known that charge trapping and recombination of injected electrons with redox species at the semiconductor–electrolyte interface might compete with carrier collection in DSSCs and reduce the overall efficiency of light-to-electric energy conversion. However, the fundamental interactions responsible for binding of redox species at the semiconductor surface and the influence of solvation and surface defects on the recombination processes remain poorly understood. This paper analyzes fundamental aspects of surface solvation in model systems of TiO<sub>2</sub>–acetonitrile interfaces, with emphasis on the description of interactions of redox species with oxygen vacancy defects at the molecular level.

The development of DSSCs, based on nanoporous TiO<sub>2</sub> thin films sensitized with ruthenium polypyridyl adsorbates, rapidly achieved light-to-electric energy conversion efficiencies as high as 10% for simulated solar irradiance.<sup>3,4</sup> Currently, the certified record efficiency of such solar cells is just above 11%, and measurements of their durability and stability indicate lifetimes exceeding 10 years under operational conditions.<sup>5</sup> However, attempts to achieve further improvements in efficiency have not been successful, partly due to the lack of understanding of some of the molecular and electronic processes that follow photoexcitation and interfacial electron transfer.

Significant research efforts have been invested in the optimization of light-harvesting, interfacial electron transfer, and electron–hole pair separation in current DSSC devices. The best

ruthenium-based sensitizer complexes,<sup>1,4,6</sup> such as the N3 and black dyes as well as some organic dyes,<sup>7</sup> yield photon-to-current conversion efficiencies (IPCE) >70% over the whole solar spectrum, and significant work has been focused on understanding these processes from a theoretical perspective.<sup>8–12</sup> However, the molecular processes involving redox species, including dye regeneration mechanisms, recombination of photoexcited electrons with oxidized adsorbates or electrolyte species (back-reaction), as well as the mechanism of electron transport in the TiO<sub>2</sub> substrate, remain poorly understood. In this paper, we focus on the interaction of redox species with nanoporous TiO<sub>2</sub> surfaces with oxygen vacancy defects solvated with acetonitrile. The study of electron transport in sintered TiO<sub>2</sub> thin films will be addressed elsewhere.

Currently, the most efficient DSSCs are based on the I<sup>−</sup>/I<sub>3</sub><sup>−</sup> redox couple dissolved in acetonitrile (ACN), a redox mediator that allows for efficient regeneration of the surface-adsorbed dyes after photoexcitation and interfacial electron transfer. The main advantage of the I<sup>−</sup>/I<sub>3</sub><sup>−</sup> pair when compared with other redox species (e.g., Co(II)/Co(III))<sup>13</sup> is that the I<sup>−</sup>/I<sub>3</sub><sup>−</sup> pair involves a two-electron redox process yielding very slow recombination kinetics.<sup>14,15</sup> In addition, the I<sup>−</sup>/I<sub>3</sub><sup>−</sup> pair exhibits low overpotentials for reduction of triiodide at the counter electrode and has sufficiently high solubility in ACN<sup>2</sup> and weak absorption of solar light.<sup>16</sup> Its main disadvantage, when compared with other redox mediators, is that the I<sup>−</sup>/I<sub>3</sub><sup>−</sup> redox potential at 0.35 V (versus the normal hydrogen electrode, NHE) leads to a large internal potential loss (e.g., 0.75 V), since the oxidation potential of typical dyes (e.g., Ru(dcbpy)<sub>2</sub> (NCS)<sub>2</sub>) are as positive as 1.1 V. It is, therefore, natural to expect that significant improvements in the overall efficiency of cells could be achieved with redox couples with more positive redox potentials, so long as their recombination kinetics is as slow as with the I<sup>−</sup>/I<sub>3</sub><sup>−</sup> couple.<sup>5</sup>

Experimental studies have analyzed the dark current induced by reduction of redox species at the photoanode–electrolyte

\* Corresponding author. E-mail: lrego@fisica.ufsc.br.

<sup>†</sup> Department of Chemistry, Universidade Federal de Santa Catarina.

<sup>‡</sup> Department of Physics, Universidade Federal de Santa Catarina.

<sup>¶</sup> Universidade Federal do Paraná.

<sup>§</sup> Comisión Nacional de Energía Atómica.

<sup>||</sup> Yale University.

interface.<sup>17–20</sup> However, the fundamental interactions responsible for binding of redox species at the TiO<sub>2</sub> surface remain to be characterized at the molecular level. Here, we investigate fundamental aspects of solvation of redox species at TiO<sub>2</sub>–ACN interfaces. Despite their foremost importance for dye sensitized solar cells, very few theoretical studies have addressed these fundamental interactions. The reported analysis thus complements earlier computational studies, in an effort to elucidate the nature of binding of redox species at TiO<sub>2</sub> surfaces and the molecular origin of the resulting recombination kinetics for the I<sup>−</sup>/I<sub>3</sub><sup>−</sup> couple.<sup>11</sup> General aspects of the resulting insight are expected to be valuable in the search of alternative electrolyte species to improve photoconversion efficiency.

The paper is organized as follows. Section 2 briefly reviews the influence of recombination dynamics on the overall photoconversion efficiency of typical DSSCs and the potential role played by redox species in the underlying recombination mechanism. Computational methods are introduced in section 3. Section 4 describes the computational structural models, including the solvent, adsorbates, and TiO<sub>2</sub>–electrolyte interface at the molecular level. Section 5 describes the interaction of redox species with the TiO<sub>2</sub>–electrolyte interface, and section 6 analyzes the electronic structure of the TiO<sub>2</sub>–electrolyte interface. The passivation of TiO<sub>2</sub> surfaces by functionalization with Lewis bases as a simple technique to prevent the interaction of redox species with the TiO<sub>2</sub> surface is explored in section 7. Finally, section 8 summarizes and concludes.

## 2. Influence of the I<sup>−</sup>/I<sub>3</sub><sup>−</sup> Redox Mediator on Cell Performance

The incident photon-to-current efficiency coefficient, IPCE =  $f\eta H$ , is determined by the product of the light-harvesting efficiency ( $f$ ), the net electron injection efficiency ( $\eta$ ), and the photocarrier collection efficiency ( $H$ ). For the dye sensitizers of interest,  $\eta = k_{\text{inj}}/(k_{\text{inj}} + k_{\text{decay}})$  is close to unit, since the interfacial electron transfer and electron–hole pair separation processes ( $k_{\text{inj}}$ ) occur within the picosecond time scale, whereas intramolecular recombination decay ( $k_{\text{decay}}$ ) takes hundreds of microseconds to occur.<sup>6,14</sup> The intramolecular decay processes, therefore, rarely affect the cell performance.

The electron collection efficiency ( $H$ ) is in practice determined by the competition between the collection of photoinjected electrons by the conducting substrate and their recombination with the oxidized forms of the redox mediator in solution (back-reaction) or with the oxidized dye. Long electron lifetimes are critical for efficient carrier collection. The electron back-reaction is responsible for the dark current that causes a decrease in the open circuit voltage of the DSSC and loss of photocurrent quantum efficiency.<sup>21–23</sup> Identification and characterization of the acceptor species in solution is of primary relevance to uncover the mechanistic events responsible for the back-reaction. The possible candidates include I<sub>3</sub><sup>−</sup>, I<sub>2</sub>, I<sub>2</sub><sup>•−</sup> and I<sup>•</sup>, but the current literature is somewhat conflicting about their roles. Unambiguous identification has not been achieved, despite almost two decades of investigation, because each of the possible acceptors can become a major player depending on the physicochemical conditions, such as illumination intensity,<sup>15,21</sup> electrolyte composition,<sup>5,6,14</sup> and even the characteristics of the sensitizer.<sup>24,25</sup>

In functioning dye-sensitized cells [I<sub>2</sub>] ≪ [I<sub>3</sub><sup>−</sup>], due to the strongly favorable equilibrium constant,  $k_{\text{eq}} \approx 10^7 \text{ M}^{-1}$ , of the reaction,  $\text{I}_2 + \text{I}^- \rightarrow \text{I}_3^-$  in acetonitrile. Under normal conditions, the recombination of photocarriers with I<sub>3</sub><sup>−</sup> dominates because of its much higher concentration. It has been proposed that the triiodide anion can complexate with the ACN molecules and

give rise to electron scavengers.<sup>16</sup> Nevertheless, the characteristic time for such recombination mechanism exceeds the ms time domain, which is the characteristic time for carrier migration across the TiO<sub>2</sub> thin film,<sup>2</sup> allowing most of the electrons to be collected at the back electrode. Therefore, the charge collection efficiency,  $H$ , in efficient DSSC is close to unit for normal solar irradiance.<sup>4</sup> Defects in the surface of the nanocrystalline TiO<sub>2</sub> and the presence of cations within the nanoparticle Helmholtz layer increase the recombination rate considerably.<sup>14,26,27</sup> In viscous ionic liquids, in which a high concentration of iodide is necessary, electron back-reaction can seriously degrade the cell efficiency,<sup>5,28</sup> indicating that the recombination rate increases with I<sub>3</sub><sup>−</sup> concentration.

The unstable radical I<sub>2</sub><sup>•−</sup> is produced by the dye regeneration reaction. It can decay via the dismutation reaction  $2\text{I}_2^{\bullet-} \rightarrow \text{I}^- + \text{I}_3^-$  or react with photoinjected carriers through the overall reaction  $\text{I}_2^{\bullet-} + e_{\text{CB}}^- \rightarrow 2\text{I}^-$ . Experiments conducted by Bauer and co-workers<sup>15</sup> report the existence of two regimes in the functioning of DSSCs, which are associated with the average number of injected carriers per particle ( $N_e$ ). Under normal illumination  $N_e \leq 1$  and  $H \approx 1$ , implying that most of the photocarriers are collected by the electrode and the decay of I<sub>2</sub><sup>•−</sup> is likely to occur via the dismutation reaction. For intense light irradiation,  $N_e > 1$ ; thus, the recombination rate becomes very high, and the IPCE drops substantially, indicating that back-reaction dominates over carrier collection. The effect is ascribed to electron trapping in defects of the TiO<sub>2</sub> nanocrystals; however, with conflicting interpretations.

Some studies support that the trapped electrons are those that recombine with the oxidized redox forms in the electrolyte, increasing the back electron transfer.<sup>15,26</sup> On the other hand, Frank and co-workers<sup>2</sup> defend the diffusion-limited model, according to which the trapped electrons increase the diffusion coefficient of photocarriers and consequently its chance to bind to an occasional iodine molecule. In conventional cells, approximately one iodine molecule exists for every 10<sup>4</sup> TiO<sub>2</sub> nanoparticles.

Green and co-workers<sup>21</sup> reported evidence that the recombination kinetics of photocarriers with I<sub>2</sub> is 2 orders of magnitude faster than the same recombination reaction with I<sub>3</sub><sup>−</sup>. The authors support the mechanism proposed by Liu et al.,<sup>22</sup> in which the overall reaction  $\text{I}_2 + 2e_{\text{CB}}^- \rightarrow 2\text{I}^-$  occurs in two steps: (i)  $\text{I}_2 + e_{\text{CB}}^- \rightarrow \text{I}_{\text{ads}} + \text{I}^-$  followed by (ii)  $\text{I}_{\text{ads}} + e_{\text{CB}}^- \rightarrow \text{I}^-$ , analogous to the reduction of iodine at the palladium counter electrode.<sup>29</sup>

The electron back-reaction is also influenced by the presence of cations and additives in the electrolyte. The presence of high concentrations of small size cations, such as Li<sup>+</sup> and Mg<sup>2+</sup>, can change the effective charge of the nanoparticle from negative to positive.<sup>14</sup> That allows the iodide anions to penetrate within the Helmholtz layer of the positively charged particles and interact with the dye molecules covering its surface, improving the dye regeneration or increasing the back-reaction transfer. The inclusion of Li<sup>+</sup> as well as 4-*tert*-butyl pyridine (4tBP) and similar additives in the electrolyte is a normal practice that generally results in improved cell performance,<sup>2,5,7,26,30,31</sup> although the full extension of their roles is still unclear.

Another important reaction process is dye regeneration. It is not the main subject of this study, but some of the results presented here can be useful for its understanding. Several experimental studies demonstrate that the regeneration of the oxidized dye is fast compared with the recombination rates. For instance, the half-time for regeneration of the N3 sensitizer in the presence 0.5 M iodide is in the range of 50 ns to 10 μs, depending on the precise composition of the electrolyte. Thus,

it can easily compete with any of the recombination processes in DSSC under normal operating conditions. The mechanism of dye regeneration has been directly monitored by time-dependent spectroscopy measurements.<sup>32–34</sup> It takes place through the formation of an intermediate complex, according to the two step reaction  $D^+ + I^- + I^- \rightarrow [D^+, I^-] + I^- \rightarrow D + I_2^-$ . The dye regeneration is strongly dependent on the cation species present in the electrolyte as well as the dye itself. It has been reported that certain dyes can increase the recombination rate. Miyashita et al.<sup>25</sup> suggest that this is due to a locally increased concentration of triiodide near the dye, whereas O'Regan et al.<sup>24</sup> defend that this is a consequence of the binding of iodine molecules to the sensitizer.

### 3. Methods

The study of TiO<sub>2</sub>–electrolyte interfaces combines several computational methods outlined in this section. The structural models are parametrized as described in section 4, with further details described in the Supporting Information document and in the sections where the models are discussed.

Molecular dynamics (MD) simulations of the TiO<sub>2</sub>–electrolyte interface were performed via molecular mechanics (MM) methods, as implemented by the GROMACS-4<sup>35</sup> and NAMD<sup>36</sup> packages. Molecular mechanics simulations were carried out for intervals up to 2 ns to generate statistically independent configurations of the system, which were used to calculate density profiles of the electrolyte, potentials of mean force (PMF), and electronic properties.

Some of the interaction parameters used in the MM simulations were obtained from the literature (references will be provided throughout the paper); however, model specific interactions were parametrized with energy potentials obtained from ab initio calculations. The Vienna Ab Initio Simulation Package,<sup>37–39</sup> VASP, and the Gaussian 03<sup>40</sup> packages were employed to generate the reference energy curves. VASP is a highly efficient simulation package for DFT studies of extended systems that is based on the plane-wave expansion of the Kohn–Sham orbitals. The VASP package was used to obtain optimized geometries of the TiO<sub>2</sub> substrate with and without surface defects. The Gaussian package is a suite of programs extensively utilized for quantum chemistry calculations at the ab initio level.

Calculations of projected density of states of the large size TiO<sub>2</sub>–electrolyte interface supercells were performed using a mixed quantum-classical method previously implemented in studies of electron injection in sensitized TiO<sub>2</sub> surfaces.<sup>9,10,12</sup> The quantum mechanical part of the method is based on a tight-binding model Hamiltonian gained from the semiempirical extended-Hückel (EH) method, which has been extensively applied in studies of molecular and periodic systems.<sup>41–43</sup> The method provides an excellent cost–benefit option for the description of quantum dynamic processes in very large systems. To improve the accuracy of the EH method, a genetic algorithm optimization procedure was used to parametrize the individual system components, such as the electronic structure of the acetonitrile molecule, the TiO<sub>2</sub> defect cluster, and the iodine/iodide molecules, taking the ab initio calculations of Gaussian 03 and the experimental literature as reference.

### 4. Structural Models

**4.1. Acetonitrile.** The model of acetonitrile (CH<sub>3</sub>CN), implemented in our molecular dynamics simulations, is the six-site interaction model shown in Figure 1, including three methyl

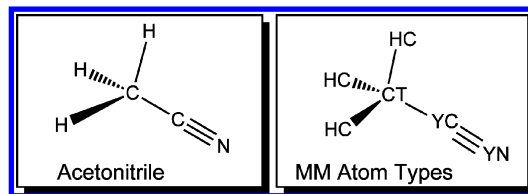


**Figure 1.** Molecular structure of acetonitrile and definition of molecular mechanics atom types.

**TABLE 1: Comparison of Average Density ( $\rho$ ) and Heat of Vaporization ( $\Delta H_{\text{vap}}$ ) Obtained by Molecular Dynamics Simulations of Liquid Acetonitrile at Room Temperature ( $T = 298$  K), Based on Model Systems Containing 216 (model 1) and 512 (model 2) ACN Molecules with Periodic Boundary Conditions**

model	$\rho$ (kg/m <sup>3</sup> )	$\Delta H_{\text{vap}}$ (kcal/mol)
1 <sup>a</sup>	760.2	7.93
2 <sup>b</sup>	753.8	7.87
exptl <sup>c</sup>	776.8	8.01

<sup>a</sup>  $P = 0.94$  bar. <sup>b</sup>  $P = 0.98$  bar. <sup>c</sup>  $P = 1.00$  bar.<sup>47</sup>

hydrogens (HC), a methyl carbon (CT), carbon (YC), and nitrogen (YN) with previously reported force field parameters.<sup>44</sup>

The model potential includes electrostatic and nonbonding pairwise additive interactions between sites  $i$  and  $j$ , including Lennard-Jones and electrostatic potentials,

$$U(r_{ij}) = 4\epsilon_{ij} \left[ \left( \frac{\sigma_{ij}}{r_{ij}} \right)^{12} - \left( \frac{\sigma_{ij}}{r_{ij}} \right)^6 \right] + \frac{q_i q_j}{r_{ij}} \quad (1)$$

where interactions between 1–4 neighbors are scaled by 0.5 and 0.83, respectively, as implemented in the AMBER molecular mechanics force field.<sup>45</sup>

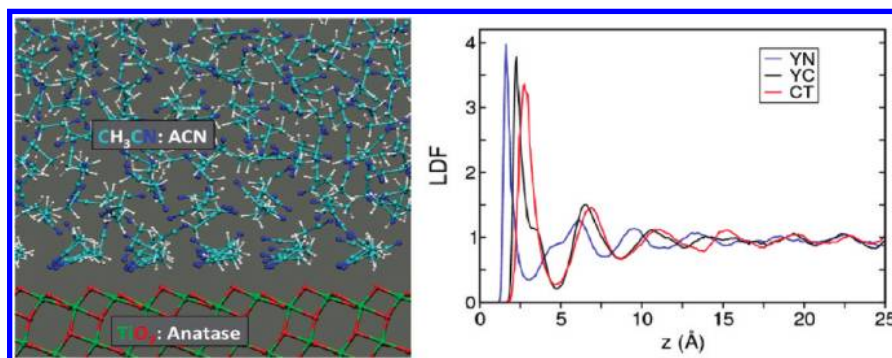
Molecular dynamics simulations involved isothermal–isobaric NPT ensembles, with 216 and 512 acetonitrile molecules in cubic boxes with periodic boundary conditions. The computational protocol for preparation, thermalization and equilibration of the system followed standard procedures,<sup>46</sup> outlined in the Supporting Information document.

Table 1 shows a comparison of calculated and experimental values of average density  $\rho$  and heat of vaporization  $\Delta H_{\text{vap}}$ , showing good agreement between the experimental and computational characterization of liquid acetonitrile.<sup>44,46</sup> Simulations for model systems with 216 and 512 ACN molecules also show good agreement with each other and with previously reported results,<sup>44</sup> including calculations of radial distribution functions.

**4.2. TiO<sub>2</sub>–Acetonitrile Interface.** Figure 2 shows a representative molecular configuration of the interface TiO<sub>2</sub> anatase (101)–acetonitrile obtained from molecular dynamics simulations performed on a  $3.1 \times 3.8 \times 4.4$  nm TiO<sub>2</sub> supercell in contact with 405 ACN molecules, with periodic boundary conditions. Simulations were based on NVT ensembles obtained after a 40 ps equilibration period. The statistical analysis of density profiles, based on 600 ps production run trajectories, shows good agreement with results reported by Schiffmann et al.<sup>48</sup> We focused on calculations of the linear density function, along the direction  $z$  normal to the interface,

$$\text{LDF}_\alpha(z) = \frac{\left\langle \sum_i \delta(z_i^\alpha - z) \right\rangle}{\rho_\alpha A_{xy}} \quad (2)$$





**Figure 2.** Representative configuration from a 600 ps MD trajectory of the TiO<sub>2</sub> anatase (101)–acetonitrile interface (left). Density profile of acetonitrile at the TiO<sub>2</sub> interface. Color key: YN (blue), YC (black), and CT (red) for atom types defined in Figure 1.

where the atom types  $\alpha = \text{YN, YC, and CT}$  are defined in Figure 1, and  $z_i^\alpha$  denotes the  $z$  coordinate of atoms  $\alpha$  at the  $i$ th molecule,  $\rho_\alpha = \langle \sum_i \delta(\mathbf{r}_i^\alpha - \mathbf{r}) \rangle$  is the equilibrium density in the bulk, and  $A_{xy}$  is the analyzed area in the  $(x, y)$  plane.

The density functions, shown in Figure 2, as well as the inspection of several representative configurations analogous to the snapshot shown in Figure 2, indicate that the ACN solvent in the vicinity of the TiO<sub>2</sub> interface is highly structured. The first ACN layer, at 1.4 Å from the first layer of the TiO<sub>2</sub> surface, is very organized, mostly due to the interactions with the 2-fold coordinate oxo bridges ( $\text{O}_{2c}^{2-}$ ) in the (101) surface and the 5-fold coordinate titanium ions,  $\text{Ti}_{5c}^{4+}$  on the surface. The orientation of ACN in this first solvation layer is such that the molecules are almost parallel to each other, making an average angle of 25° with respect to the (101) surface, with the YN type atoms of ACN pointing predominantly toward the neighboring  $\text{Ti}_{5c}^{4+}$  ions. The second layer is at ~2.8 Å from the TiO<sub>2</sub> surface, with the ACN molecules also tending to align parallel to each other, although forming a much less organized layer. Note in Figure 2 that the shoulder to the left of the second YN (blue) peak and the shoulders to the right of the first YC (black) and CT (red) peaks in the LDF data indicate that the ACN molecules in the second solvation layer tend to align antiparallel to those in the first layer. The CT atoms of ACN in the first layer nearly overlap with the CT atoms of the second layer, giving rise to a broad peak centered at 2.5 Å.

In all of our calculations, the interactions between ACN and the TiO<sub>2</sub> surface were described by Lennard-Jones potential with force field parameters reported by Schiffmann, Hutter, and VandeVondele.<sup>48</sup> The TiO<sub>2</sub> structure was kept fixed at the DFT equilibrium configuration, obtained with the VASP package,<sup>37</sup> as previously reported.<sup>9</sup> These DFT calculations applied the generalized gradient approximation, together with the Perdew–Wang (PW91) exchange–correlation functional and ultrasoft pseudopotentials.

**4.3. Oxygen Vacancy Defects: Influence on the TiO<sub>2</sub>–Acetonitrile Interface.** Figure 3 shows a TiO<sub>2</sub> cluster with an oxygen vacancy defect, obtained by conjugate gradient geometry optimization as implemented in the VASP package at the DFT level, using GGA and the Perdew–Wang exchange–correlation functional. This is one of the most common stoichiometric defects of TiO<sub>2</sub> surfaces, leading to changes in the structural and electronic properties of the material by formation of localized electron traps (i.e.,  $\text{Ti}^{3+}$  states) in the semiconductor band gap. Here, we analyze the structural and electronic nature of the defect (Figure 3) and its influence on the structure of the solvent at the TiO<sub>2</sub>–acetonitrile interface (Figure 4).

The oxygen vacancy model was built by relaxing the structure of a  $[\text{TiO}_2]_{64}$  supercell with periodic boundary conditions after

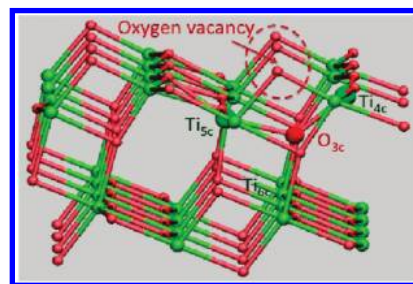


**Figure 3.** Relaxed DFT–PW91 configuration of a TiO<sub>2</sub>–anatase surface (101) with a surface defect oxygen vacancy. The lattice sites most displaced, during surface reconstruction induced by the surface defect, are highlighted with enlarged spheres, including  $\text{O}_{3c}$ ,  $\text{Ti}_{5c}$ , and  $\text{Ti}_{4c}$  atoms. Color key: O (red), Ti (green).

removing a 2-fold coordinate oxo bridge ( $\text{O}_{2c}^{2-}$ ) from the (101) surface. The resulting surface reconstruction, shown in Figure 3, involves displacement of the 3-fold  $\text{O}_{2c}^{2-}$  ion coordinated to the pentacoordinated  $\text{Ti}_{5c}^{4+}$ , at (1.98 Å), as well as displacement of the tetracoordinated  $\text{Ti}_{4c}^{3+}$  at (1.82 Å) and to the  $\text{Ti}_{6c}^{4+}$  at (2.14 Å). These displacements correspond to a  $\text{Ti}_{5c}$ – $\text{O}_{3c}$ – $\text{Ti}_{4c}$  angle of ~125° and define a relaxed configuration in very good agreement with earlier DFT–GGA calculations, based on the Perdew–Burke–Ernzerhof (PBE) semilocal exchange–correlation functional.<sup>49,50</sup>

Having developed a model of a TiO<sub>2</sub>–anatase slab with oxygen vacancy defects, we analyzed the influence of surface defects on the structure of the solvent in close contact with the TiO<sub>2</sub> surface. Figure 4 shows a representative configuration of the anatase–ACN interface, including  $\text{O}_{2c}$  vacancies in the (101) surface. Figure 4 shows that ACN molecules approach the TiO<sub>2</sub> surface as Lewis base moieties, with the lone pairs of the N atoms (blue) interacting with Ti ions at the surface.

Figure 4 shows the ACN density functions for the anatase/ACN system with  $\text{O}_{2c}$  oxygen vacancies. When compared with the corresponding ACN density functions for pristine surfaces (shown in Figure 2), one of the most significant differences is that the density function for the N of ACN (i.e., atom type YN) now has a peak at short distances (i.e., at ~1 Å from the  $\text{O}_{2c}$  plane of atoms) not seen for pristine surfaces. Such a peak is consistent with the picture of ACN molecules approaching the oxygen vacancy defect at the TiO<sub>2</sub> surface and interacting as Lewis base moieties with the N in close contact with the defect, as shown in the representative configuration of the solvent in ACN–TiO<sub>2</sub> defect (left panel). It is, therefore, natural to conclude that the TiO<sub>2</sub> nanoparticles typically used in DSSC, that are never perfectly stoichiometric, have surface defects due to oxygen vacancies that affect not only the structural and electronic properties of the substrate but also the properties of the ACN solvent in close contact with the surface.

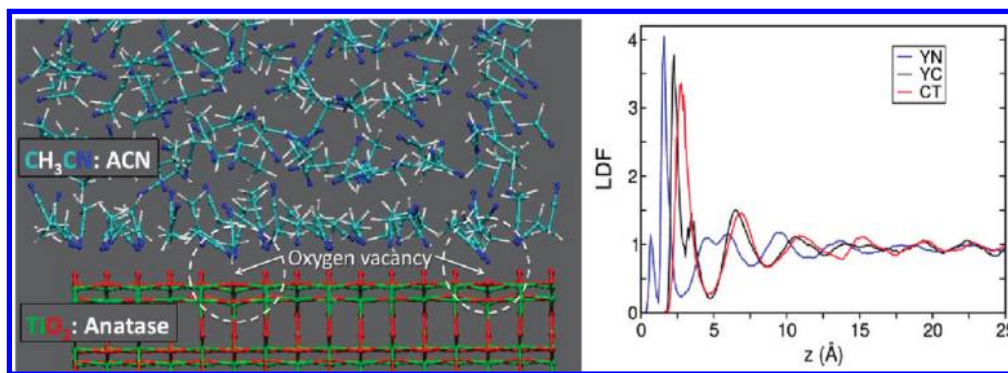


**Figure 4.** (Left) Representative configuration of ACN solvent in contact with a (101) TiO<sub>2</sub>–anatase surface, with surface oxygen vacancy defects. Color key: O (red), Ti (green), C (light blue), N (blue), H (white). (Right) Linear density profiles for the TiO<sub>2</sub>/ACN interface with oxygen vacancy defects. The peaks correspond to atom types YN (blue), YC (black), and CT (red), defined in Figure 1.

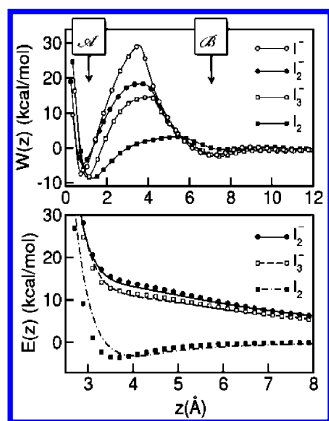


**Figure 5.** Top panel: Potential of mean force  $W(z)$  describing the effective interactions between  $I_3^-$ ,  $I_2^-$ ,  $I_2$ , and  $I^-$  in ACN and the TiO<sub>2</sub> surface at the vicinity of an oxygen vacancy defect. Bottom panel: Comparison of ab initio potential energy surfaces between a TiO<sub>2</sub> H<sub>6</sub> cluster and redox species, including  $I_3^-$  (dashed line),  $I_2^-$  (solid line) and  $I_2$  (dotted–dashed line). Calculations based on the molecular mechanics force field described in the text are shown by symbols.

## 5. Redox Species

**5.1. Binding Interactions at the TiO<sub>2</sub>/Acetonitrile Interface.** Figure 5 shows the comparative analysis of the effective potential of interaction between the TiO<sub>2</sub> surface and redox species in solution, including  $I_3^-$ ,  $I_2^-$ ,  $I^-$ , and  $I_2$  in ACN at 0.1 M concentration (i.e.,  $\sim 1$ – $2$  ions dissolved in 400–430 ACN molecules). We focus on the analysis of interactions at the vicinity of an oxygen vacancy defect, as characterized by the potential of mean force  $W(z)$ , defined as follows,

$$W(z) \propto k_B T \ln \langle \delta(z_\alpha - z) \rangle \quad (3)$$

where  $z_\alpha$  denotes the  $z$  coordinate, normal to the TiO<sub>2</sub>–anatase surface (101), measured from the vacant O<sub>2c</sub> site to the closest site in the solute. The expression  $\langle \dots \rangle$ , introduced by eq 3, denotes the statistical average obtained from room temperature molecular dynamics simulations.

The potentials of mean force exhibit minimum energy configurations at  $z \sim 1$  Å, corresponding to adsorptive states  $\mathcal{A}$ , where the redox species are tightly adsorbed to oxygen vacancy defects in the Stern layer. States  $\mathcal{A}$  are more stable than the fully solvated state of the corresponding redox species in the bulk, suggesting that surface defects are effective electron traps occupied by redox species. The analysis of thermal configurations for states  $\mathcal{A}$  indicates that the ions orient themselves almost parallel to the interface at the surface defect

(see Figure 6). In the absence of redox species, such sites are typically occupied by solvent molecules (e.g., ACN as shown in Figure 4). Local minimum energy configurations are observed at  $z \sim 7.2$  Å, corresponding to marginally bound states  $\mathcal{B}$  in the outer Helmholtz layer.

Figure 5 shows that states  $\mathcal{A}$  and  $\mathcal{B}$  are separated by large free-energy barriers, computed by using an adaptive force bias scheme implemented in the NAMD code.<sup>51</sup> As shown in Figure 5 (top panel), transferring redox species from  $\mathcal{B}$  to  $\mathcal{A}$  requires surmounting free-energy barriers of  $\Delta W(\mathcal{B} - \text{peak}) \approx 17$ , 20, and 32 kcal mol<sup>−1</sup> for  $I_3^-$ ,  $I_2^-$ , and  $I^-$ , respectively. Desorbing redox species from  $\mathcal{A}$  by transferring them to state  $\mathcal{B}$  is even more difficult, with free energy barriers  $\Delta W(\mathcal{A} - \text{peak}) \approx 23$  kcal mol<sup>−1</sup> for both  $I_3^-$  and  $I_2^-$ , and  $\Delta W(\mathcal{A} - \text{peak}) \approx 35$  kcal mol<sup>−1</sup> for  $I^-$ .

The underlying dynamics of interconversion between states  $\mathcal{A}$  and  $\mathcal{B}$  is characterized by the “forward” and “reverse” rate constants,  $k_f(\mathcal{A} \rightarrow \mathcal{B})$  and  $k_r(\mathcal{A} \leftarrow \mathcal{B})$ , respectively, estimated by transition state theory.<sup>52</sup> The Arrhenius rate  $k_r$  for transferring redox species from  $\mathcal{B}$  to  $\mathcal{A}$  is

$$k_r \approx \frac{D}{kT} \frac{\sqrt{|W''_{\text{peak}}| \cdot W''_{\mathcal{B}}}}{2\pi} \exp[-\beta \Delta W_{\mathcal{B}}] \quad (4)$$

where  $\mu = eD/kT$  is the ionic mobility in the solvent and  $(|W''_{\text{peak}}| \cdot W''_{\mathcal{B}})^{1/2}$  is the geometric mean of second derivatives at the minimum and maximum of  $W(z)$ . Considering the diffusion constant to be  $D \approx 1.3 \times 10^{-5}$  cm<sup>2</sup>/s for both anionic species,<sup>53</sup> we obtain the prefactor of eq 4, approximately equal for both anions, yielding

$$k_r(I_3^-) \approx (1 \times 10^{11} \text{ s}^{-1}) e^{-17/0.596} \approx 4 \times 10^{-2} \text{ s}^{-1}$$

$$k_r(I_2^-) \approx (1 \times 10^{11} \text{ s}^{-1}) e^{-20/0.596} \approx 3 \times 10^{-4} \text{ s}^{-1}$$

The profile of the potential of mean force  $W(z)$  for neutral  $I_2$  is significantly different from the corresponding profiles of the ionic species. The position of the minimum next to the oxygen vacancy is shifted away from the surface, and the activation free energy barrier, separating states  $\mathcal{A}$  and  $\mathcal{B}$ , is significantly lower than the corresponding barriers for ionic species. In addition, the activation free-energy barrier for desorption from  $\mathcal{B}$  into the bulk is significantly lower and comparable to typical thermal energies  $\Delta W_{\mathcal{B}} \sim 1$ – $2$  kcal/mol.

The molecular mechanics force field parameters, characterizing the interactions between TiO<sub>2</sub> and redox species, were



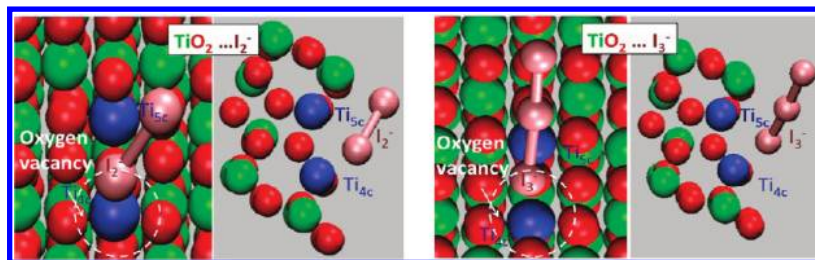


**Figure 6.** Configuration of  $I_2^-$  (left) and  $I_3^-$  (right) adsorbed to an  $O_{2c}$  vacancy site at the  $TiO_2/ACN$  interface. The  $Ti_{4c}$  and  $Ti_{5c}$  ions at the defect are depicted in blue; other titanium ions are shown in green, and oxygen is in red. For clarity, solvating ACN molecules are not shown.

obtained by fitting the ab initio potential energy profile computed at the MP2/LanL2DZ level of quantum chemistry with Gaussian 03<sup>40</sup> to an effective Lennard-Jones plus Coulomb potential  $E(z)$  (Figure 5, lower panel). Considering the preferential orientation of the adsorbate species, relative to the substrate, we analyzed the approach of the solute species to a  $TiO_5H_6$  cluster, following a path in which the axis of ionic species remained perpendicular to the anatase surface. The fitting procedure yields Lennard-Jones parameters  $\sigma_{Ti-I} = 2.16$  Å,  $\sigma_{O-I} = 3.24$  Å,  $\epsilon_{Ti-I} = 3.15$  kcal mol<sup>-1</sup>, and  $\epsilon_{O-I} = 0.94$  kcal/mol. Partial charges at the  $I_3^-$  were chosen to be  $-0.4865e$  ( $-0.03e$ ) for the external (internal) sites,<sup>54</sup> whereas the intramolecular site–site distances in the solutes were set to the equilibrium distances of the solute species in vacuo, obtained from a similar ab initio estimate; namely,  $d_{I_3} = 3.140$  Å,  $d_{I_2} = 3.407$  Å, and  $d_{I_2} = 2.877$ . Molecular parameters for the interactions between the ionic species and ACN were taken from ref 54, assuming the usual arithmetic and geometrical means. Figure 5 (lower panel) shows the agreement between potential energy curves  $E(z)$  obtained by using the resulting molecular mechanics force field as compared with ab initio MP2 calculations. We find that the force field reproduces well the repulsive characteristics of the potential energy between the cluster and ionic species as well as the attractive branch of the neutral  $I_2$  potential energy curve.

The comparisons between the potentials of mean force  $W(z)$  for solvated redox species interacting with  $TiO_2$  and the potential energy curves  $E(z)$  for the corresponding species interacting with the dry  $TiO_5H_6$  cluster provides fundamental insights into the origin of the activation energy barriers for adsorption/desorption of redox species to an oxygen vacancy defect. Since barriers are not observed for  $E(z)$ , the barriers in  $W(z)$  must be due to free-energy changes in desolvation of the solutes when changing from the polar, bulklike, outer Helmholtz layer in the  $\mathcal{B}$  states to the adsorbed states  $\mathcal{A}$  in the Stern layer. Such free energy changes are a lot more pronounced for the charged redox species (i.e.,  $I_2^-$ ,  $I^-$ , or  $I_3^-$ ) than for the neutral  $I_2$  molecule. This hypothesis is additionally supported by the relative heights of free energy barriers. In particular, the adsorption of  $I^-$ , where the net charge is localized in a single site, leads to a maximum solvation energy change and demonstrates that the origin of the barriers can be traced back to modifications in the solvation structure prevailing in bulklike states. In contrast, the more delocalized charges in  $I_2^-$  and  $I_3^-$  lead to a weaker solute–solvent Coulomb coupling and, consequently, lower free energy barriers.

## 6. Electronic Structure

Figures 7 and 8 analyze the electronic structure of the  $TiO_2$ –electrolyte interface in terms of the density of electronic states, projected onto the orbitals of the constituent molecular fragments. The model includes a  $[TiO_2]_{384}$  supercell cluster with 12  $O_{2c}$  vacancy defects, 432 ACN solvent molecules, and the  $I_2$  or  $I_3^-$  redox species. The analysis is focused on the effect of

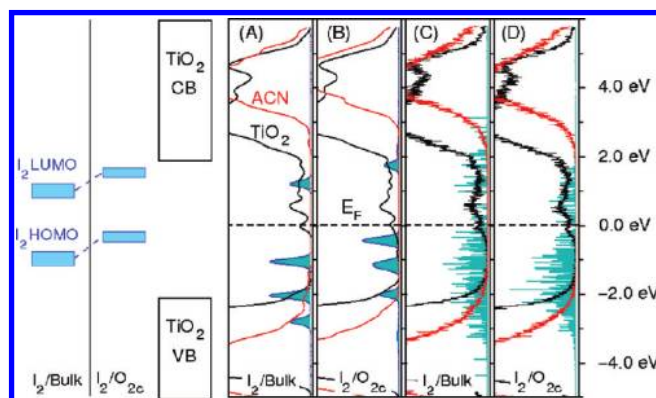


**Figure 7.** Projected density of states for the  $TiO_2/I_2^-/ACN$  interface, including the projection into  $TiO_2$  states (black), ACN (red) and  $I_2^-$  (blue, scale  $\times 20$ ). The Fermi level is set to zero. Panels A and B correspond to two representative configurations with  $I_2^-$  in the bulk of ACN (A) or adsorbed to an oxygen vacancy defect (B), with individual peaks broadened by a Gaussian with fwhm = 100 mV. Panels C and D are the corresponding averages of the PDOS from an ensemble of configurations sampled from room temperature molecular dynamics simulations. The diagram on the left depicts the energy shifts of the  $I_2^-$  frontier orbitals.

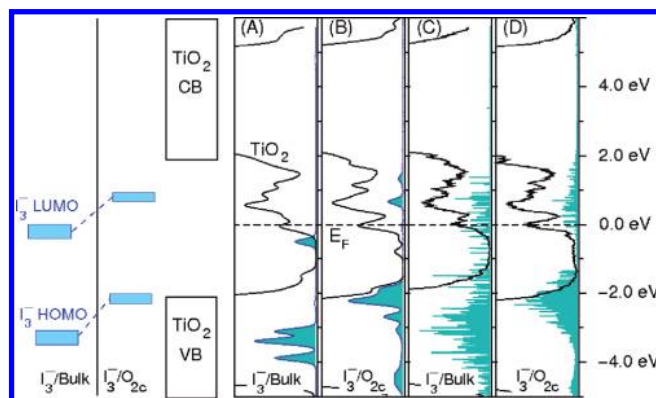


**Figure 8.** Projected density of states for the  $TiO_2/I_3^-/ACN$  interface, including the projection into  $TiO_2$  states (black) and  $I_3^-$  (blue, scale  $\times 5$ ). The Fermi level is set to zero. Panels A and B correspond to two representative configurations with  $I_3^-$  in the bulk of ACN (A), or adsorbed to an oxygen vacancy defect (B), with individual peaks broadened by a Gaussian with fwhm = 100 mV. Panels C and D are the corresponding averages of the PDOS from an ensemble of configurations sampled from room temperature molecular dynamics simulations. The diagram on the left depicts the energy shifts of the  $I_3^-$  frontier orbitals.

oxygen vacancy defects and the properties of redox species adsorbed to the  $TiO_2$  surface as compared with the corresponding electronic properties of the species dissolved in the bulk solvent (i.e., with  $I_2$  or  $I_3^-$  sufficiently far from the  $TiO_2$  surface).

The density of electronic states projected onto  $TiO_2$  orbitals shows the conduction and valence bands of the anatase  $TiO_2$  (black lines), separated by a gap of  $\sim 3.5$  eV, and the defect

states occupying a region of 1–2 eV below the conduction band. Two broad peaks describe the bonding and antibonding bands of the acetonitrile (red lines), separated by a gap of  $\sim 8.5$  eV. The calculated Fermi level is located at the onset of the defect states in the gap. The atomic configurations were obtained from the MD simulations, and two types of analysis were performed: the regular PDOS calculations (panels A and B) are made for one typical snapshot with Gaussian broadening of the individual peaks, whereas the  $\langle$ PDOS $\rangle$  calculations (panels C and D) are configuration averages carried over 200 MD snapshots.

To study the interaction of the redox species with the TiO<sub>2</sub> surface, panels A and C of Figure 7 describe the I<sub>2</sub> molecule in the bulk of the solvent and far from the interface. The calculations reveal that the degeneracy of the I<sub>2</sub> molecular orbitals is well preserved (panel A), but the position of the peaks fluctuates a lot (panel C) due to the interaction of the solute with the solvent molecules and variations on the I<sub>2</sub> bond length.

The interaction between the I<sub>2</sub> molecule and the TiO<sub>2</sub> defect is described by panels B and D. In this case, the MD simulations show that the redox species is hovering steadily over a defect site between the TiO<sub>2</sub> surface and the first solvent layer. That decreases the fluctuation of the I<sub>2</sub> molecular orbital energies. The left side of Figure 7 describes the average energy shift of the I<sub>2</sub> molecular orbitals relative to the TiO<sub>2</sub> levels. The HOMO and LUMO states of the iodine molecule are shifted to higher energies while the energy of the defect site is shifted to slightly lower values. The fact that the TiO<sub>2</sub> surface protects the I<sub>2</sub> molecule from the solvation effect of the ACN molecules contributes to the big energy shift of the frontier orbitals of the molecule. Typically, the HOMO moves to the border of the Fermi level of the nanoparticle, occasionally crossing it due to solvent fluctuations. That could lead to a charge transfer between the two systems and, possibly, adsorption followed by dissociation of the I<sub>2</sub> molecule. Our calculations, therefore, support the two-step dissociative mechanism proposed by Liu et al.<sup>22</sup> and also observed by Green and co-workers.<sup>21</sup>

Figure 8 describes the density of electronic states for the triiodide anion in the vicinity of the interface. For the sake of clarity, we do not show the projected density of states (PDOS) curve of the solvent in Figure 8, since it repeats the behavior of Figure 7. Panel A shows the frontier orbitals of the I<sub>3</sub><sup>−</sup> molecule when it is in the bulk of the solvent and far from the surface, for a typical MD snapshot, and panel C shows the configurational average. The high mobility of the triiodide anion is reflected in the wide distribution of the I<sub>3</sub><sup>−</sup> peaks in the  $\langle$ PDOS $\rangle$  calculation. Once the I<sub>3</sub><sup>−</sup> overcomes the barrier of the ACN solvation layer and binds to a defect site, the triiodide dwells very steadily over the defect, even more than the I<sub>2</sub> molecule. That is reflected in the relatively narrow PDOS peak distribution shown in Figure 8D. The interaction between the I<sub>3</sub><sup>−</sup> anion and the O<sub>2c</sub> defect is qualitatively described by the energy diagram on the left-hand side. In this case, the HOMO lies well below the Fermi level of the TiO<sub>2</sub>. Therefore, the recombination of photoexcited electrons in the nanoparticle with the I<sub>3</sub><sup>−</sup> anion should take place by the transfer of the photoelectron to the LUMO of the triiodide as it approaches the surface and crosses the free energy barrier, shown in Figure 5.

The calculations of the projected density of states are based on a tight binding model Hamiltonian gained from the semiempirical Extended Hückel (EH) method, implemented in the basis of Slater-type orbitals (STO) for the radial part of the atomic orbital wave functions.<sup>55</sup> The overlap and the off-diagonal Hamiltonian matrix elements are computed, respectively, as  $S_{ij} = \langle \psi_i | \psi_j \rangle$  and  $H_{ij}^0 = \kappa S_{ij} (H_{ii}^0 + H_{jj}^0)/2$ . Once the semiempirical

parametrization was performed for the constituent systems individually (i.e., the reduced TiO<sub>2</sub> cluster, the ACN molecule, and the redox species), no energy shifts or further corrections were necessary for either the occupied or unoccupied states of the interface system, since the diagonal elements of the Hückel Hamiltonian,  $H_{ii}^0$ , correspond approximately to the valence state ionization potential of the atomic species.

Long-range interactions were also taken into account, since acetonitrile is a polar solvent. The dipole fields produced by the ACN molecules shift the energy levels of the redox pair as well as the energies of the TiO<sub>2</sub> surface states, which are mainly located on the edge of the conduction and valence bands. Instead of using a continuum model for the solvent, which is not a good approximation near the interface, we apply an atomistic method. The potential  $\Phi(\vec{r})$  due to the polar molecules is  $\Phi(\vec{r}) = \sum_k \langle \vec{\mu}_k \rangle \cdot (\vec{r} - \vec{R}_k) / |\vec{r} - \vec{R}_k|^3$ , where  $\vec{R}_k$  is the barycenter of nuclear charge on the  $k$ th solvent molecule and  $\langle \vec{\mu}_k \rangle = -\sum_i^{\text{occ}} \langle \psi_i | e \vec{r}_k | \psi_i \rangle$  is the electronic dipole moment, with  $\vec{r}_k = \vec{r} - \vec{R}_k$ . The matrix elements of the dipole potential  $\Phi(\vec{r})$ , between two Slater-type atomic orbitals is given approximately by  $\Phi_{ij} = \int \psi_i(\vec{r}) \Phi(\vec{r}) \psi_j(\vec{r}) d\vec{r} \approx S_{ij} \Phi((\vec{R}_i + \vec{R}_j)/2)$ , where  $S_{ij}$  is the overlap matrix element and  $\vec{R}_i$  is the position of atom  $i$ . Thus, the Hamiltonian that incorporates the dielectric effects of the solvent is rewritten as  $H_{ij} = H_{ij}^0 - e\Phi_{ij}$ , where  $H_{ij}^0$  are the matrix elements of the plain EH Hamiltonian. The solvent shift calculated for the molecular orbitals of the I<sub>2</sub> molecule is  $\sim 0.7$  eV, according to this approach.

Due to its semiempirical nature, judicious use and proper parametrization are essential for applying the EH method. Therefore, we generated a new set of parameters for each of the constituent systems of the interface by means of a genetic algorithm optimization procedure, in which the parameters characterizing the radial part of the Slater-type orbitals and the Wolfsberg–Helmholz parameter itself were allowed to vary. The criteria utilized for the new parametrization included the transition energies among frontier orbitals, Mülliken population analysis, the dipole moment, and the symmetry of the molecular orbitals. The reference data were taken from experimental results and from ab initio calculations performed with the Gaussian package. The optimized parameters are provided as Supporting Information. The procedure was applied for the I<sub>2</sub>, I<sub>3</sub><sup>−</sup>, and ACN molecules in vacuo. The optimized parameters were then transferred for the quantum calculations of the interface system, producing results in accordance with the literature.<sup>16,56,57</sup>

The reduction of TiO<sub>2</sub> by oxygen vacancies produces Ti<sup>3+</sup> ions in the surface and subsurface layers of the nanoparticle.<sup>50</sup> Such n-type defects give rise to excess electrons occupying the 3d orbitals of the Ti atoms neighboring the vacancy. It is believed that the defect states produce localized unpaired spin states around 1 eV below the CB. Experimental evidence of such defect states in TiO<sub>2</sub> include the appearance of an absorption band in the visible<sup>58,59</sup> and electron paramagnetic resonance signals of the unpaired electrons.<sup>60</sup> It has been demonstrated that plain DFT–GGA methods are inadequate to describe such localized states, since DFT has the tendency of delocalizing unpaired electron states to reduce self-interaction. The problem can be partially solved with the use of DFT+U approaches or hybrid functional methods (like the Becke 3-parameter Lee–Yang–Parr, B3LYP), in which the Hartree–Fock exchange is mixed with DFT exchange.<sup>61–64</sup> However, there is no fundamental principle to determine the values of the U parameter, which can vary from 2 to 4 eV in this case, nor the amount of mixture in hybrid functionals, rendering both



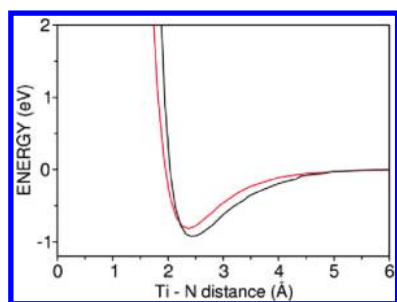


**Figure 9.** Comparison of the pyridine–TiO<sub>2</sub> interaction potential as described by the ab initio DFT (red) and molecular mechanics (black) models.

methods somewhat empirical too. Moreover, the nature of the defect states depends strongly on the methods used.<sup>64</sup>

In our framework, we parametrized only the 3d levels of the Ti<sub>5c</sub> and Ti<sub>4c</sub> ions around the defect site, leaving the other atomic levels unaltered. By doing that, states were created in the gap, 1–2 eV below the CB, which are strongly localized on the 3d levels of the reduced Ti atoms neighboring the O<sub>2c</sub> vacancy.

## 7. Passivation of TiO<sub>2</sub> Surfaces

In an earlier study, we have shown that Lewis base moieties can block oxygen vacancy defects on TiO<sub>2</sub> surfaces.<sup>65</sup> Here, we focus on the passivation of TiO<sub>2</sub> surfaces by adsorption of pyridine-like moieties, under room temperature conditions, with emphasis on the characterization of the resulting interface structure at the molecular level.

**7.1. Pyridine–TiO<sub>2</sub> Model.** Pyridine (Py) and pyridine-derivatized compounds, such as the 4*t*BP, are frequently used as additives to improve the efficiency of the DSSC.<sup>30</sup> It is generally believed that the additive molecules adsorb on the surface of the nanoparticle and isolate it from the electrolyte. Its presence also shifts the conduction band to lower binding energies by ~0.2 eV.<sup>7,30,59,66</sup> Pyridine adsorbs on anatase standing up, with its N atom oriented toward the Ti<sub>5c</sub> atoms of the surface. In reduced TiO<sub>2</sub> samples, pyridine-based compounds bind preferably to surface oxygen vacancies on both Ti<sub>5c</sub> and oxygen vacancy sites.<sup>59</sup> Geometry optimization at the ab initio level<sup>67</sup> for the TiO<sub>2</sub>–pyridine system has been made for systems constituted of just one pyridine molecule on a TiO<sub>2</sub> cluster in vacuo. Such studies obtained an adsorption energy of 28.3 kcal/mol and an equilibrium Ti–N distance of 2.34 Å.

In our MD simulations, the internal structure of the pyridine is described by the AMBER force field. To describe the TiO<sub>2</sub>–pyridine interaction, nonbonding Lennard-Jones FF parameters were derived for the interaction between the N atom of pyridine and the Ti<sub>5c</sub> of the pristine TiO<sub>2</sub> surface, which is the main interaction for the adsorption of Py on anatase, together with Coulombic potentials with the O<sub>2c</sub> atoms. The Lennard-Jones parameters were obtained, as described in the Supporting Information document, by fitting the DFT-PW91 potential energy surface computed with the VASP package for the pyridine–[TiO<sub>2</sub>]<sub>64</sub> system as a function of the Ti<sub>5c</sub>–N distance and average orientation of pyridine relative to the Ti<sub>5c</sub> center on the surface. Both curves are shown in Figure 9, and the obtained parameters are  $\sigma_{\text{Ti-N}} = 1.175$  Å and  $\epsilon_{\text{Ti-N}} = 4.09$  kJ/mol. In the process of deriving the FF parameters, in addition to the overall fitting of the adsorption curve, the mean Ti–N distance as well as the orientation of the pyridine molecule were also taken into account.

Molecular dynamics simulations explored different levels of surface coverage for pyridine on anatase (101) surfaces in vacuo

or solvated with ACN. Thermalization and equilibration simulation procedures consisted of ramping the temperature of the TiO<sub>2</sub>–pyridine system from 10 to 298 K in the NVT ensemble, for an interval of 50 ps, followed by MD simulations at  $T = 298$  K for intervals of 2 ns.

**7.2. Pyridine Binding to TiO<sub>2</sub>–Anatase.** Figure 10 shows representative configurations gained from molecular dynamics simulations of pyridine moieties adsorbed on a TiO<sub>2</sub>–anatase surface (101), revealing two main orientations for pyridine adsorbed on anatase, including a longitudinal orientation along the  $[\bar{1}01]$  direction (observed at low surface coverage) and an oblique orientation that gives rise to a herringbone-like arrangement under high surface coverage conditions (see Figure 10). In both orientations, pyridine molecules adsorb to the TiO<sub>2</sub> surface as typical Lewis base moieties, with the N group directly coordinated to the Ti<sub>5c</sub> ions. The average Ti<sub>5c</sub>–N distances are 2.42 and 2.30 Å for the aligned and oblique orientations, respectively.

These results are consistent with earlier studies, including Kusama's ab initio calculations of a pyridine molecule on a TiO<sub>2</sub> cluster in vacuo,<sup>67</sup> reporting an adsorption energy of 28.3 kcal/mol and an equilibrium Ti–N distance of 2.34 Å as well as a recent study of TiO<sub>2</sub> samples in which pyridine-based compounds were found to bind preferably to Ti<sub>5c</sub> and oxygen vacancy sites.<sup>59</sup> The agreement with earlier studies gives support to the parametrization of the model and molecular dynamics simulations, with the internal structure of pyridine described by the AMBER force field,<sup>45</sup> and the TiO<sub>2</sub>–pyridine interactions described by a combination of Lennard-Jones and Coulombic potentials.

The reported results also support the generally accepted model of passivation of TiO<sub>2</sub> thin films by functionalization with pyridine-derivatized compounds (e.g., 4-*tert*-butyl pyridinium (4*t*BP)). This is a standard procedure, usually applied in the preparation of DSSCs after dye sensitization of the TiO<sub>2</sub> thin films.

**7.3. TiO<sub>2</sub>/Pyridine–Acetonitrile Interface.** Figure 11 shows a representative configuration of the TiO<sub>2</sub>–anatase surface (101) saturated with pyridine and solvated with acetonitrile molecules, as obtained by molecular dynamics simulations at room temperature with periodic boundary conditions.

At high surface coverage, pyridine moieties adopt a herringbone arrangement, as discussed in Section 7.2 (see Figure 10). Starting from an initial configuration in which pyridine moieties are aligned along the  $[101]$  direction, the pyridine adsorbates equilibrate with the ACN solvent and rearrange into the herringbone configuration within a few tens of picoseconds, fluctuating in that average orientation for the remainder of the simulation period. The pyridine adsorbate molecules form an insulating monolayer, ~7 Å thick, around the nanoparticle surface that is stable at room temperature, even in contact with the acetonitrile solvent.

The structure of the pyridine monolayer is also evident from the quantitative analysis provided by the linear density functions (Figure 11, right panel). In contrast to the density profiles of ACN in direct contact with TiO<sub>2</sub> (Figures 2 and 4), Figure 11 shows that the first ACN solvation layer is at ~7 Å from the TiO<sub>2</sub> surface, since the pyridine adsorbates saturate the surface and prevent close contact interactions between the solvent and TiO<sub>2</sub>. Another important difference between the structure of ACN in contact with the TiO<sub>2</sub>–pyridine surface and in contact with bare TiO<sub>2</sub> is that, in the first case, the ACN molecules orient themselves parallel to the TiO<sub>2</sub>–pyridine surface (Figure 11, left panel), but in direct contact with TiO<sub>2</sub> (Figures 2 and

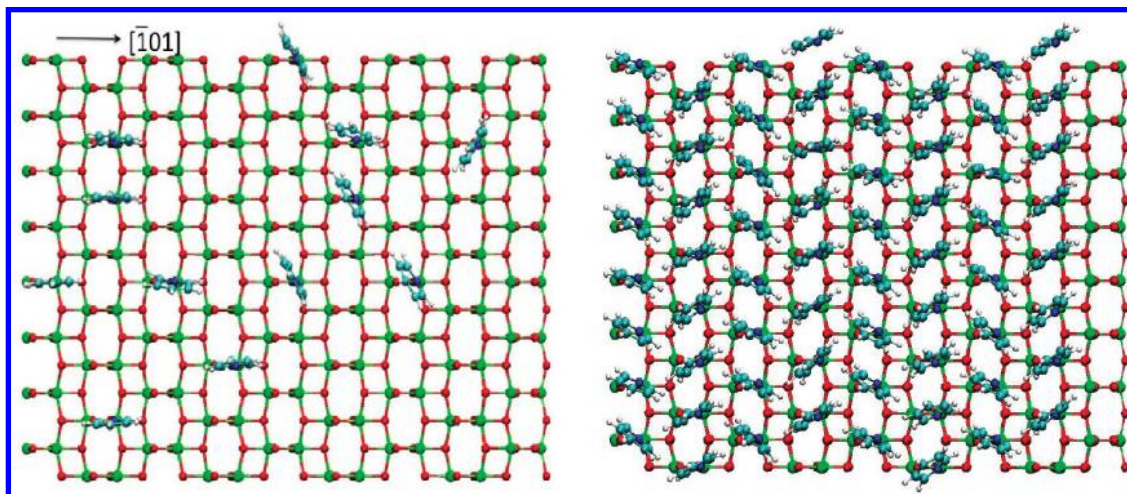


**Figure 10.** Representative configurations of the TiO<sub>2</sub>–anatase surface (101), functionalized with pyridine molecules at low surface coverage (left) and maximum coverage (right), as obtained from room temperature molecular dynamics simulations. At high concentrations, the adsorbed pyridine adopt the herringbone type configuration. Color key: O (red), Ti (green), C (light blue), N (blue), H (white).

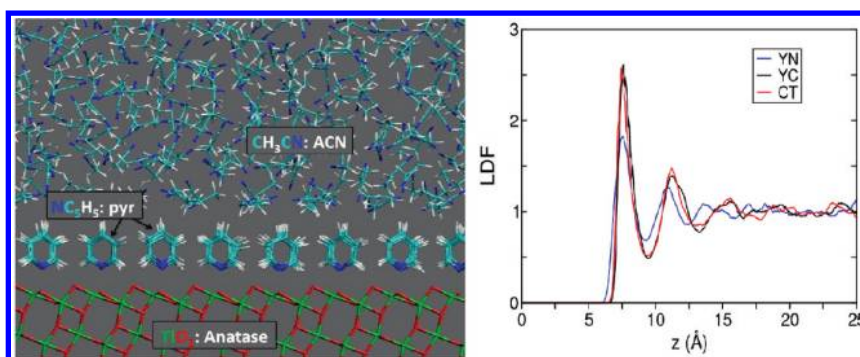


**Figure 11.** (Left) Representative configuration of a TiO<sub>2</sub>–anatase surface (101) completely saturated with pyridine moieties and solvated by acetonitrile. (Right) Linear density functions for ACN along the direction normal to the semiconductor/solvent interface.

4), the ACN molecules form a double layer with an average antiparallel orientation. Consistently, with our computational results and several experimental studies,<sup>2,5,7,26,30,31</sup> it is thought that the 4rBP moieties adsorb to the TiO<sub>2</sub> surface as Lewis base species. The resulting functionalization passivates the surface by sterically hindering close contact interactions between redox species and the TiO<sub>2</sub> surface, suppressing detrimental recombination processes due to electron transfer with redox species in solution (back-electron transfer).

## 8. Conclusions

A comprehensive study of the TiO<sub>2</sub>–electrolyte interface was presented. The investigation of the structural properties revealed that the surface of the TiO<sub>2</sub> nanoparticle is solvated by a well organized layer of ACN molecules, with its nitrogen atom oriented toward the Ti<sub>5c</sub> atoms of the TiO<sub>2</sub> surface. At defect sites, produced by the vacancy of O<sub>2c</sub> atoms, the N–Ti interaction is further increased, and the solvent advances into the vacancy site.

Free-energy calculations for the advance of redox species toward the nanoparticle surface demonstrated the existence of an energy barrier of ~15–20 kcal/mol for the anionic species and a stable energy minimum at the defect site, between the TiO<sub>2</sub> surface and the first solvation layer. The adsorption rate  $k(I_3^-) \approx 4 \times 10^{-2} \text{ s}^{-1}$  was estimated from the free energy potential.

The analysis of the electronic structure of the TiO<sub>2</sub>/redox/ACN system shows that the HOMO and LUMO orbitals of the

redox species are shifted to higher energies by crossing the ACN solvation layer. The effect suggests the occurrence of distinct recombination mechanisms with the different redox species. For the I<sub>2</sub> molecule, the HOMO approaches the Fermi level of the nanoparticle, occasionally crossing it due to solvent fluctuations. In this case, the results support the two-step dissociative mechanism<sup>22</sup> for back-reaction. On the other hand, recombination photoelectrons with I<sub>3</sub><sup>−</sup> should occur via electron transfer to the LUMO of the anion as it crosses the solvation barrier. Although the present study provides a deeper insight on the molecular mechanisms taking place at the TiO<sub>2</sub>–electrolyte interface, the calculations should be corroborated in the future by more rigorous theoretical procedures and experimental measurements.

The effect of organic additives was investigated by introducing pyridine molecules in the system. The simulations indicate that pyridine binds strongly to pentacoordinated Ti<sub>5c</sub> ions and efficiently hinder the approach of ACN molecules to the surface.

**Acknowledgment.** The authors thank the joint project CNPq-CONICET-NSF for collaboration in Materials Science. L.G.C.R. and R.S. acknowledge financial support from CNPq/Brazil. D.L. and J.R. are staff members of CONICET-Argentina. V.S.B. acknowledges supercomputer time from NERSC and support from NSF grants CHE-0911520 and ECCS-040419, and from the Division of Chemical Sciences, Geosciences, and Biosciences, Office of Basic Energy Sciences of the U.S. Department of Energy (DE-FG02-07ER15909).



**Supporting Information Available:** Additional technical documentation on computational methods and parametrization of the tight-binding model Hamiltonians. This material is available free of charge via the Internet at <http://pubs.acs.org>.

## References and Notes

- (1) Hodes, G. *Electrochemistry of Nanomaterials*; Wiley-VCH: New York, 2001.
- (2) Frank, A. J.; Kopidakis, N.; van de Lagemaat, J. *Coord. Chem. Rev.* **2004**, *248*, 1165–1179.
- (3) O'Regan, B.; Grätzel, M. *Nature* **1991**, *353*, 737–740.
- (4) Hagfeldt, A.; Grätzel, M. *Acc. Chem. Res.* **2000**, *33*, 269–277.
- (5) Boschloo, G.; Hagfeldt, A. *Acc. Chem. Res.* **2009**, *42*, 1819–1826.
- (6) Ardo, S.; Meyer, G. J. *Chem. Soc. Rev.* **2009**, *38*, 115–164.
- (7) Hara, K.; Dan-oh, Y.; Kasada, C.; Ohga, Y.; Shinpo, A.; Suga, S.; Sayama, K.; Arakawa, H. *Langmuir* **2004**, *20*, 4205–4210.
- (8) (a) Ernstorfer, R.; Gundlach, L.; Felber, S.; Storck, W.; Eichberger, R.; Willig, F. J. *Phys. Chem. B* **2006**, *110*, 25383–25391. (b) Gundlach, L.; Ernstorfer, R.; Willig, F. *Prog. Surf. Sci.* **2007**, *82*, 355–377. (c) Wang, L.; Willig, F.; May, V. J. *Chem. Phys.* **2007**, *126*, 134110, (1–12).
- (9) Rego, L. G. C.; Batista, V. S. J. *Am. Chem. Soc.* **2003**, *125*, 7989–7997.
- (10) Abuarbara, S. G.; Rego, L. G. C.; Batista, V. S. J. *Am. Chem. Soc.* **2005**, *127*, 18234–18242.
- (11) Duncan, W. R.; Craig, C. F.; Prezhdo, O. V. J. *Am. Chem. Soc.* **2007**, *129*, 8528–8543.
- (12) Rego, L. G. C.; Silva, R.; Freire, J. A.; Snoeberger, R. C., III; Batista, V. S. J. *Phys. Chem. C* **2010**, *114*, 1317–1325.
- (13) Nusbaumer, H.; Moser, J. E.; Zakeeruddin, S. M.; Nazeeruddin, M. K.; Grätzel, M. J. *Phys. Chem. B* **2001**, *105*, 10461–10464.
- (14) Pelet, S.; Moser, J. E.; Grätzel, M. J. *Phys. Chem. B* **2000**, *104*, 1791–1795.
- (15) Bauer, C.; Boschloo, G.; Muhktar, E.; Hagfeldt, A. J. *Phys. Chem. B* **2002**, *106*, 12693–12704.
- (16) Kebede, Z.; Lindquist, S.-E. *Sol. Energy Mater. Sol. Cells* **1999**, *57*, 259–275.
- (17) Huang, S. Y.; Schlichthorl, G.; Nozik, A. J.; Grätzel, M.; Frank, A. J. J. *Phys. Chem. B* **1997**, *101*, 2576–2582.
- (18) Liu, Y.; Hagfeldt, A.; Xiao, X.-R.; Lindquist, S.-E. *Sol. Energy Mater. Sol. Cells* **1998**, *55*, 267–281.
- (19) Schlichthorl, G.; Huang, S. Y.; Sprague, J.; Frank, A. J. J. *Phys. Chem. B* **1997**, *101*, 8139–8153.
- (20) Nakade, S.; Kanzaki, T.; Kubo, W.; Kitamura, T.; Wada, Y.; Yanagida, S. J. *Phys. Chem. B* **2005**, *109*, 3480–3487.
- (21) Green, A. N. M.; Chandler, R. E.; Haque, S. A.; Nelson, J.; Durrant, J. R. J. *Phys. Chem. B* **2005**, *109*, 142–150.
- (22) Liu, Y.; Hagfeldt, A.; Xiao, X. R.; Lindquist, S.-E. *Sol. Energy Mater. Sol. Cells* **1998**, *55*, 267–281.
- (23) Huang, S. Y.; Schlichthorl, G.; Nozik, A. J.; Grätzel, M.; Frank, A. J. J. *Phys. Chem. B* **1997**, *101*, 2576–2582.
- (24) O'Regan, B. C.; Durrant, J. A. *Acc. Chem. Res.* **2009**, *42*, 1799–1808.
- (25) Miyashita, M.; Sunahara, K.; Nishikawa, T.; Uemura, Y.; Koumura, N.; Hara, K.; Mori, A.; Abe, T.; Suzuki, E.; Mori, S. J. *Am. Chem. Soc.* **2008**, *130*, 17874–17881.
- (26) Haque, S. A.; Tachibana, Y.; Willis, R. L.; Moser, J. E.; Grätzel, M.; Klug, D. R.; Durrant, J. R. J. *Phys. Chem. B* **2000**, *104*, 538–547.
- (27) Kambe, S.; Nakade, S.; Kitamura, T.; Wada, Y.; Yanagida, S. J. *Phys. Chem. B* **2002**, *106*, 2967–2972.
- (28) Paulsson, H.; Klooa, L.; Hagfeldt, A.; Boschloo, G. J. *Electroanal. Chem.* **2006**, *586*, 56–61.
- (29) Bay, L.; West, K.; Jensen, B. W.; Jacobson, T. *Sol. Energy Mater. Sol. Cells* **2006**, *90*, 341–351.
- (30) Dürr, M.; Yasuda, A.; Nelles, G. *Appl. Phys. Lett.* **2006**, *89*, 061110: 1–3.
- (31) Nazeeruddin, M. K.; Kay, A.; Rodicio, I.; Baker, R. H.; Mueller, E.; Liska, P.; Vlachopoulos, N.; Grätzel, M. J. *Am. Chem. Soc.* **1993**, *115*, 6382–6390.
- (32) Peter, L. M. J. *Phys. Chem. B* **2007**, *111*, 6601–6612.
- (33) Nasr, C.; Hotchandani, S.; Kamat, P. V. J. *Phys. Chem. B* **1998**, *102*, 4944–4951.
- (34) Clifford, J. N.; Palomares, E.; Nazeeruddin, M. K.; Grätzel, M.; Durrant, J. R. J. *Phys. Chem. C* **2007**, *111*, 6561–6567.
- (35) Hess, B.; Kutzner, C.; van der Spoel, D.; Lindahl, E. J. *Chem. Theory Comput.* **2008**, *4*, 435–447.
- (36) Phillips, J. C.; Braun, R.; Wang, W.; Gumbart, J.; Tajkorsheid, E.; Villa, E.; Chipot, E.; Skeel, R. D.; Kalé, L.; Schulten, K. J. *Comput. Chem.* **2005**, *26*, 1781–1802.
- (37) Kresse, G.; Furthmüller, J. *Vienna ab initio Simulation Package (VASP)*; University of Vienna: Vienna, Austria, 2001.
- (38) Kresse, G.; Furthmüller, J. *Comput. Mater. Sci.* **1996**, *6*, 15–50.
- (39) Hafner, J. *Comput. Phys. Commun.* **2007**, *177*, 6–13.
- (40) Frisch, M. J.; Trucks, G. W.; Schlegel, H. B.; Scuseria, G. E.; Robb, M. A.; Cheeseman, J. R.; Montgomery, J. A., Jr.; Vreven, T.; Kudin, K. N.; Burant, J. C.; Millam, J. M.; Iyengar, S. S.; Tomasi, J.; Barone, V.; Mennucci, B.; Cossi, M.; Scalmani, G.; Rega, N.; Petersson, G. A.; Nakatsuji, H.; Hada, M.; Ehara, M.; Toyota, K.; Fukuda, R.; Hasegawa, J.; Ishida, M.; Nakajima, T.; Honda, Y.; Kitao, O.; Nakai, H.; Klene, M.; Li, X.; Knox, J. E.; Hratchian, H. P.; Cross, J. B.; Bakken, V.; Adamo, C.; Jaramillo, J.; Gomperts, R.; Stratmann, R. E.; Yazyev, O.; Austin, A. J.; Cammi, R.; Pomelli, C.; Ochterski, J. W.; Ayala, P. Y.; Morokuma, K.; Voth, G. A.; Salvador, P.; Dannenberg, J. J.; Zakrzewski, V. G.; Dapprich, S.; Daniels, A. D.; Strain, M. C.; Farkas, O.; Malick, D. K.; Rabuck, A. D.; Raghavachari, K.; Foresman, J. B.; Ortiz, J. V.; Cui, Q.; Baboul, A. G.; Clifford, S.; Cioslowski, J.; Stefanov, B. B.; Liu, G.; Liashenko, A.; Piskorz, P.; Komaromi, I.; Martin, R. L.; Fox, D. J.; Keith, T.; Al-Laham, M. A.; Peng, C. Y.; Nanayakkara, A.; Challacombe, M.; Gill, P. M. W.; Johnson, B.; Chen, W.; Wong, M. W.; Gonzalez, C.; Pople, J. A. *Gaussian 03, revision C02*; Gaussian, Inc.: Wallingford CT, 2004.
- (41) Hoffman, R. *Rev. Mod. Phys.* **1988**, *60*, 601–628.
- (42) Burdett, J. K. *Chemical Bonding in Solids*; Oxford Press: Oxford, 1995.
- (43) Cerdá, J. S. *Phys. Rev. B* **2000**, *61*, 7965–7971.
- (44) Nikitin, A. M.; Lyubartsev, A. P. J. *Comput. Chem.* **2007**, *28*, 2020–2026.
- (45) Cornell, W. D.; Cieplak, P.; Bayly, C. I.; Gould, I. R.; Merz, K. M.; Ferguson, D. M.; Spellmeyer, D. C.; Fox, T.; Caldwell, J. W.; Kollman, P. A. J. *Am. Chem. Soc.* **1995**, *117*, 5179–5197.
- (46) Grabuleda, X.; Jaime, C.; Kollman, P. A. J. *Comput. Chem.* **2000**, *21*, 901–908.
- (47) An, X. M.; Mansson, M. J. J. *Chem. Thermodyn.* **1983**, *15*, 287–293.
- (48) Schiffrmann, F.; Hutter, J.; VandeVondele, J. J. *Phys.: Condens. Matter* **2008**, *20*, 64206.
- (49) Tilloca, A.; Selloni, A. J. *Chem. Phys.* **2003**, *119*, 7445–7450.
- (50) Cheng, H.; Selloni, A. *Phys. Rev. B* **2009**, *79*, 092101-1:4.
- (51) (a) Darve, E.; Pohorille, A. J. *Chem. Phys.* **2001**, *115*, 9169. (b) Chipot, C.; Hémin, J. J. *Chem. Phys.* **2005**, *123*, 244906.
- (52) Gardiner, C. W. *Handbook of Stochastic Methods*, 3rd ed.; Springer-Verlag: Berlin, 2003.
- (53) Hauch, A.; Georg, A. *Electrochim. Acta* **2001**, *46*, 3457–3466.
- (54) Zhang, F. S.; Lyndell-Bell, R. M. *Eur. J. Phys. D* **2005**, *34*, 129.
- (55) McGlynn, S. P.; Vanquickenborne, L. G.; Kinoshita, M.; Carroll, D. G. *Introduction to Applied Quantum Chemistry*; Holt, Rinehart and Winston, Inc.: New York, 1972.
- (56) (a) Leach, S.; Schwell, M.; Un, S.; Jochims, H. W.; Baumgärtel, H. *Chem. Phys.* **2008**, *344*, 147–163. (b) Mota, F. B.; Rivelino, R. J. *Phys. Chem. B* **2009**, *113*, 9489–9492.
- (57) Pathak, A. K.; Mukherjee, T.; Maity, D. K. J. *Chem. Phys. A* **2010**, *114*, 721–724.
- (58) Khomenko, V. M.; Langer, K.; Rager, H.; Fett, A. *Phys. Chem. Miner.* **1998**, *25*, 338.
- (59) Yu, S.; Ahmadi, S.; Sun, C.; Palmgren, P.; Hennies, F.; Zuleta, M.; Göthelid, M. J. *Phys. Chem. C* **2010**, *114*, 2315–2320.
- (60) Zhou, S.; Cizmar, E.; Poztger, K.; Krause, M.; Talut, G.; Helm, M.; Fassbender, J.; Zvyagin, S. A.; Wosnitza, J.; Schmidt, H. *Phys. Rev. B* **2009**, *79*, 113201-1:4.
- (61) Valentini, C. D.; Paachioni, G.; Selloni, A. *Phys. Rev. Lett.* **2006**, *97*, 166803.
- (62) Morgan, B. J.; Watson, G. W. J. *Phys. Chem.* **2010**, *114*, 2321–2328.
- (63) Yang, K.; Dai, Y.; Huang, B.; Feng, Y. P. *Phys. Rev. B* **2010**, *81*, 033202-1:4.
- (64) Finazzi, E.; Valentin, C. D.; Pacchioni, G.; Selloni, A. J. *Chem. Phys.* **2008**, *129*, 154113.
- (65) McNamara, W. R.; Snoeberger, R. C.; Li, G.; Schleicher, J. M.; Cady, C. W.; Poyatos, M.; Schmuttenmaer, C. A.; Crabtree, R. H.; Brudvig, G. W.; Batista, V. S. J. *Am. Chem. Soc.* **2008**, *130*, 14329–14338.
- (66) Shi, C.; Dai, S.; Wang, K.; Pan, X.; Kong, F.; Hu, L. *Vib. Spectrosc.* **2005**, *39*, 99–105.
- (67) Kusama, H.; Orita, H.; Sugihara, H. *Langmuir* **2008**, *24*, 4411–4419.